Remote Sensing of Environment 178 (2016) 113–126

Contents lists available at ScienceDirect

Remote Sensing of Environment

journal homepage: www.elsevier.com/locate/rse

Mapping macroalgal blooms in the Yellow Sea and East China Sea using HJ-1 and Landsat data: Application of a virtual baseline reflectance height technique

Qianguo Xing [a,*], Chuanmin Hu [b]

[a] Key Laboratory of Coastal Environmental Processes and Ecological Remediation, Yantai Institute of Coastal Zone Research, Chinese Academy of Sciences, 17 Chunhui Road, Laishan District, Yantai, Shandong 264003, China
[b] College of Marine Science, University of South Florida, 140 Seventh Avenue, South, St. Petersburg, FL 33701, USA

ARTICLE INFO

Article history:
Received 9 April 2015
Received in revised form 5 January 2016
Accepted 25 February 2016
Available online 16 March 2016

Keywords:
VB-FAH
FAI
NDVI
Green tide
Ulva prolifera
HJ-1
Landsat
TM
ETM+
Yellow Sea
East China Sea

ABSTRACT

Several methods have been proposed in previous studies to map macroalgal blooms (MABs) in the Yellow Sea (YS) and East China Sea (ECS), yet some of the required spectral bands are not available on the new HJ-1 satellite sensors although they do provide optimal resolution and temporal coverage (30-m resolution with 2-day revisit frequency) for bloom mapping. In this study, an index of Virtual-Baseline Floating macroAlgae Height (VB-FAH) is proposed to use the green and red bands as the baseline to measure the height of the near-infrared (NIR) reflectance. Cross-sensor comparison with Landsat TM and ETM+ data suggests that for several images evaluated here VB-FAH appears to be comparable to the previously proposed Floating Algae Index (FAI) even in the absence of a shortwave-infrared (SWIR) band. VB-FAH is applied to 30-m resolution TM and ETM+ data for the YS during 1995–2006 and to HJ-1 data for the ECS during 2009–2014 to map MABs. Results show bloom history in the YS back to 1999 and early bloom occurrence in the ECS in winter and spring (e.g., February and March 2013). MABs are also found to extend to the ECS as far south as 26°N near Fujian Province and Taiwan, and as far east as the Kuroshio Current. These new findings provide important information for exploring the origins, causes, and consequences of MABs in the YS and ECS.

1. Introduction

Macroalgal blooms (MABs) of various types have been reported to have increased in recent years in the global oceans (Gower, Young, & King, 2013; Smetacek & Zingone, 2013), with both ecological and economic implications (Lyons, Arvanitidis, Blight, Chatzinikolaou, Guy-Haim, Kotta, Orav-Kotta, Queirós, Rilov, Somerfield, & Crowe, 2014). In the Yellow Sea (YS), the world's largest MABs of *Ulva prolifera* were first reported in summer 2008 (Hu & He, 2008; Xing, Loisel, Schmitt, Shi, Liu, & Keesing, 2009), and several follow-on studies documented their occurrence in every summer as early as 2000 (Hu, Li, Chen, Ge, Muller-Karger, Liu, Yu, & He, 2010; Xing, Zheng, Shi, Hao, Yu, Liang, Liu, & Zhang, 2011, Xing, Tosi, Braga, Gao, & Gao, 2015a; Cui, Zhang, Sun, Jia, Zhao, Wang, & Meng, 2013). These MABs are thought to initiate from coastal waters off Jiangsu Province (China), and experience rapid growth under favorable conditions (light and nutrient availability) (Liu, Keesing, Xing, & Shi, 2009; Hu, Li, Chen, Ge, Muller-Karger, Liu, Yu, & He, 2010; Pang, Liu, Shan, Xu, Zhang, Gao, Chopin, & Sun, 2010; Xing, Liu, Liang, Yu, & Shi, 2010; Xing, Tosi, Braga, Gao, & Gao, 2015a). It has been proposed that the recent expansion of the seaweed — "nori" aquaculture led to the recurrent MABs since 2008, as farmers simply discarded the green macroalgae in water after harvesting seaweeds by the end of April (Liu, Keesing, Xing, & Shi, 2009; Hu, Li, Chen, Ge, Muller-Karger, Liu, Yu, & He, 2010; China Ocean News, CON, 2013). Preliminary results through satellite observations showed the trend of progressive eutrophication in the YS that was possibly linked to the MABs (Xing, Zheng, Shi, Hao, Yu, Liang, Liu, & Zhang, 2011, Xing, Tosi, Braga, Gao, & Gao, 2015a). Yet, to date, the exact history, causes, and consequences of MABs (Xing, Hu, Tang, Tian, Tang, Wang, Lou, & Gao, 2015b) in the YS and East China Sea (ECS) are still poorly understood.

Accurate mapping of MABs is a prerequisite for any subsequent studies at synoptic scales. Since the first use of the Moderate Resolution Imaging Spectroradiometer (MODIS) satellite instruments to detect and trace MABs in the YS (Hu & He, 2008), several studies have also used MODIS to map MABs and document their spatial and temporal distributions (Xing, Loisel, Schmitt, Shi, Liu, & Keesing, 2009; Xing, Zheng, Shi, Hao, Yu, Liang, Liu, & Zhang, 2011, Xing, Tosi, Braga, Gao, & Gao, 2015a; Liu, Keesing, Xing, & Shi, 2009; Hu, Li, Chen, Ge, Muller-Karger,

* Corresponding author.
E-mail addresses: qgxing@yic.ac.cn, qgxing@yahoo.com (Q. Xing).

http://dx.doi.org/10.1016/j.rse.2016.02.065
0034-4257/

Liu, Yu, & He, 2010). The MODIS image series show that the MABs drifted south in early May from turbid waters near the northern Jiangsu Shoal to the ESC, and this represents a new transport pathway in addition to the northward drifting associated with the SuBei Coastal Current (SBCC) along the coast of northern Jiangsu Province (Xing, Zheng, Shi, Hao, Yu, Liang, Liu, & Zhang, 2011).

The use of MODIS and the Medium Resolution Imaging Spectrometer (MERIS) in the previous studies (Hu & He, 2008; Xing, Loisel, Schmitt, Shi, Liu, & Keesing, 2009; Hu, Li, Chen, Ge, Muller-Karger, Liu, Yu, & He, 2010; Son, Min, & Ryu, 2012; Gower, Young, & King, 2013) provided frequent mapping capacity because of their wide satellite swath width, yet their relatively coarse resolution (250–300 m) may have missed the small patches of MABs. In contrast, although Landsat TM and ETM+ sensors have much narrower swath and lower revisit frequency, their finer resolution (30 m) could detect small macroalgae patches that would not show up in MODIS or MERIS imagery. The combined use of Landsat and MODIS images revealed the spatial and temporal distribution patterns of MABs between the end of April and July in the YS, and some of the blooms were also found in the ECS (Hu, Li, Chen, Ge, Muller-Karger, Liu, Yu, & He, 2010; Xing, Zheng, Shi, Hao, Yu, Liang, Liu, & Zhang, 2011).

Although the first reported large-scale MABs occurred in 2007 and some macroalgae slicks were found back in 2000 (Hu, Li, Chen, Ge, Muller-Karger, Liu, Yu, & He, 2010; Xing, Zheng, Shi, Hao, Yu, Liang, Liu, & Zhang, 2011), several key questions remain to be addressed, for example: what's the earliest month of MAB occurrence? What's the earliest year of MAB occurrence? Have MABs occurred in other regions of the ECS that have not been reported in the published works? These questions have been difficult to address with either MODIS or Landsat data alone, as they have either coarse resolution or low revisit frequency. Thus, the objective of this study is to complement the MODIS and Landsat observations through the use of two new satellite sensors with fine resolution (30-m) and high revisit frequency (2-day). These sensors, however, were designed mainly for land use and therefore are not equipped with a spectral band deemed critical in the Floating Algae Index (FAI) algorithm to detect and quantify MABs (Hu, 2009). Therefore, a first task would be to develop a new model in the absence of such a band.

The structure of the manuscript is as follows. The characteristics of the new sensor are introduced first, followed by the development of the new model for detecting and quantifying MABs. Then, the model is applied to time-series of satellite data to address the above questions.

2. Data sources

2.1. Field data

The study area of the YS and the ECS (25–37°N, 119–127°E) are marginal seas of the Pacific Ocean characterized by east-Asian Monsoons. In winter, surface water along the Jiangsu coast moves from the YS to the ECS (Su, 1998; Naimie, Blain, & Lynch, 2001), and in summer the water movement is reversed. The month of May is the transition month when water movement is slow (Naimie, Blain, & Lynch, 2001). The Jiangsu Shoal (JS), the origin of floating macroalgae, is featured by radially-shaped tidal ridges and high concentrations of suspended sediments. Annual mean Chl-a concentration, as derived by MODIS, is higher in the YS than in the ECS (Fig. 1a).

The field data were collected mainly to understand the spectral characteristics of the MABs in order to help design remote sensing algorithms. In situ reflectance of living floating macroalgae were measured on 26 June 2010 (Fig. 1b) and 23 June 2014 when MABs arrived in coastal waters off Qingdao. A fiber-optic probe with a 10° field of view connecting to a portable spectroradiometer (USB4000, Ocean Optics, Inc.) was pointed vertically 1 m over the sea surface to record the radiance of macroalgae (L_a, DN), and then pointed to a reference plaque with a calibrated reflectance of 0.25 to record the radiance of the plaque (L_p, DN); this procedure was repeated three times for every set of measurements to determine the mean L_a and L_p. Reflectance of macroalgae was calculated as R (unitless) $= L_a * 0.25/L_p$. Several examples of the measured reflectance spectra are shown in Fig. 1c.

2.2. Satellite data

Two Chinese satellites, namely HJ-1A and HJ-1B, can provide 30-m resolution data with a two-day revisit cycle. While the resolution is the same as with Landsat, the combination of HJ-1A and HJ-1B (every two days) is 4 times more efficient than the combination of Landsat-5 and Landsat-7 (or Landsat-7 and landsat-8, every 8 days). However, HJ-1A and HJ-1B only provide data after 2009. HJ-1A and HJ-1B have 4 bands similar to the first 4 bands of Landsat-5 TM and Landsat-7 ETM+. The characteristics of these bands are listed in Table 1.

Because MABs in April and May have been reported previously (Hu, Li, Chen, Ge, Muller-Karger, Liu, Yu, & He, 2010; Xing, Zheng, Shi, Hao, Yu, Liang, Liu, & Zhang, 2011; Hu, Yang, Zhang, Chen, & He, 2014), in this study HJ-1 images over the ECS were used to detect possible early MABs from January to March (2009–2014). Similarly, because large-scale MABs since 2007 in the YS were documented with MODIS data (Hu, Li, Chen, Ge, Muller-Karger, Liu, Yu, & He, 2010; Xing, Tosi, Braga, Gao, & Gao, 2015a), in this study Landsat images were used to study the history of MABs before 2007 in the YS (1995–2006).

A total of 66 Landsat images and 63 HJ-1 images with <50% cloud cover obtained from the United States Geological Survey (USGS) and the China Centre for Resources Satellite Data and Application (CRESDA), respectively, were used, whose coverage is shown in Fig. 1. These data were geo-referenced with land and clouds masked. The ENVI™ FLAASH (Fast Line of sight Atmospheric Analysis of Spectral Hypercubes) atmospheric correction module was applied to Landsat and HJ-1 images to derive the sea surface reflectance (R, unitless). FLAASH includes a method for aerosol estimation based on the dark pixel reflectance ratio method (Kaufman, Wald, Remer, Gao, Li, & Flynn, 1997), which has been successfully used in the atmospheric correction of multi-band or hyperspectral images over waters (e.g., Kutser, Pierson, Kallio, Reinart, & Sobek, 2004; Kutser, 2012; Tian, Lu, Chen, Yu, Xiao, Qiu, & Zhao, 2010; Moses, Gitelson, Perk, Gurlin, Rundquist, Leavitt, Barrow, & Brakhage, 2012; Zeng, Zhao, Tian, & Chen, 2013). The requirement of absolute accuracy of atmospheric correction in this study, however, is not critical because it is the relative height of the near-infrared band that is used for detecting and quantifying macroalgae.

2.3. Evaluation of cross-sensor consistency

In this study, several measures were used to compare the indices derived from two types of different sensors (HJ-1 and Landsat) or any two different indices from each of the two sensors. These include the coefficient of determination (R^2), the unbiased percent difference (UPD, Eq. (1)), and the mean relative difference (MRD, Eq. (2)).

$$UPD(\%) = \frac{1}{N}\sum_{i=1}^{N}\frac{|(y_i - x_i)|}{0.5 * (|y_i| + |x_i|)} * 100 \quad (1)$$

$$MRD(\%) = \frac{1}{N}\sum_{i=1}^{N}\frac{|(y_i - x_i)|}{|x_i|} * 100 \quad (2)$$

where y and x are either two different indices from the same image or the same index from two images collected by two different sensors (HJ-1 and Landsat). While the UPD provides an absolute difference between two sensors (a measure of data scattering) and the use of two-sensor average in the denominator is to put the same weight on both sensors (Barnes & Hu, 2015), the MRD represents an index for relative mean bias. Furthermore, to reduce mis-matching caused by

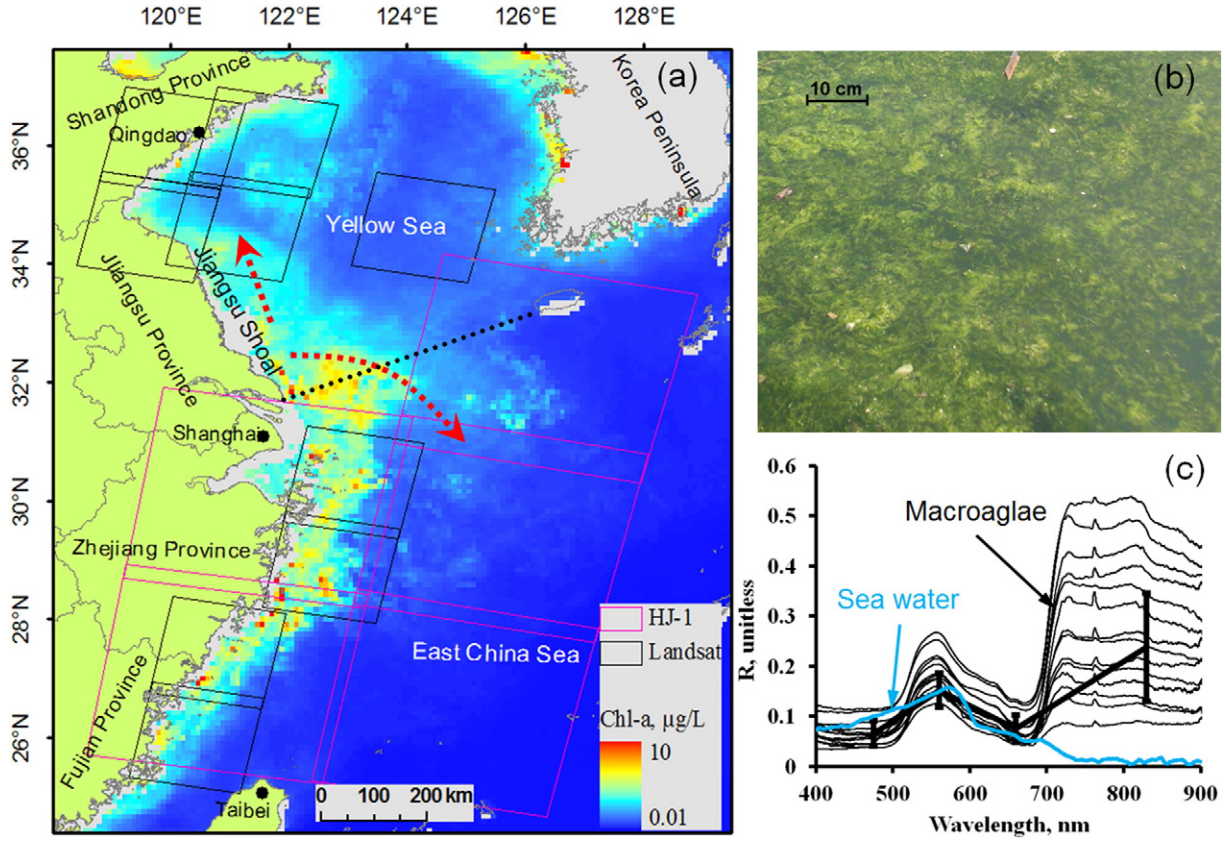

Fig. 1. (a) Study area showing the YS and ECS, separated by the black dotted line. The red arrows show the surface currents at the Jiangsu Shoal (JS) in summer and winter, respectively (Naimie, Blain, & Lynch, 2001). The red and black boxes show the coverage of HJ-1 and Landsat images, respectively, used in this study. The background MODIS/Aqua image shows the Chlorophyll-a concentration in 2006 (Source: NASA, http://oceancolor.gsfc.nasa.gov/); (b) A photo of the *Ulva prolifera* macroalgae mat taken on 26 June 2010 in Qingdao coastal waters; (c) Reflectance spectra of the macroalgae mat and sea water, with the bold black line showing the mean reflectance of macroalgae corresponding to the 4 HJ-1 bands and the first 4 bands of Landsat-5 and Landsat-7. "$_{\top}$" is for standard deviation (S.D.).

currents, waves and swells, and image registration errors between the two satellite overpasses, the 30-m resolution HJ and Landsat reflectance images were binned to 930-m resolution using a running window of 31 * 31 pixels after trial-and-error experiments. A smaller window size would induce the image-image mis-matching effects due to the factors above, while a larger window size would smear the macroalgae reflectance feature. Such derived HJ-1 and Landsat image pairs were used to analyse the cross-sensor consistency with the UPD and MRD.

Table 1
Characteristics of Landsat and HJ-1 30-m bands.

Band #	Wavelength, µm		
	HJ-1A/CCD, HJ-1B/CCD	Landsat-5/TM, Lansat-7/ETM+	Landsat-8/OLI
1	0.43–0.52 µm	0.45–0.52 µm	0.43–0.45 µm
2	0.52–0.60 µm	0.52–0.60 µm	0.45–0.52 µm
3	0.63–0.69 µm	0.63–0.69 µm	0.53–0.60 µm
4	0.76–0.90 µm	0.76–0.90 µm	0.64–0.67 µm
5	–	1.55–1.75 µm	0.85–0.89 µm
6	–	–	1.56–1.66 µm
7	–	2.08–2.35 µm	2.10–2.30 µm
8	–	–	–
9	–	–	1.36–1.39 µm
Swath	360 km	180 km	180 km
Revisit cycle	4 days (2 days for HJ-1 constellation)	16 days	16 days
Data period	2009–present	Landsat-5, 1984–2011 Lansat-7, 1999-	2013–present

"–" means no band or no 30-m band.

3. Development of a multi-sensor index for Landsat and HJ-1

3.1. Floating macroalgae and VB-FAH index

Several indices have been proposed and used by the research community to map vegetative cover. Among these, the concept of NDVI (Normalized Difference Vegetation Index, Eq. (3), Rouse, Haas, Schell, & Deering, 1973) is perhaps the most widely used index. The reflectance of floating macroalgae (Fig. 1c) is generally similar to that of land vegetation with the typical red-edge reflectance, therefore could be mapped by NDVI (Hu & He, 2008). However, using radiative transfer simulations and image comparisons, Hu (2009) showed that NDVI was sensitive to perturbations by aerosols and variable solar/viewing geometry as well as other factors (e.g., thin clouds) when used to map floating macroalgae.

$$NDVI = (R_{NIR} - R_{RED})/(R_{NIR} + R_{RED}). \quad (3)$$

The Enhanced Vegetation Index (EVI, Eq. 4) was introduced by Huete & Justice (1999) to enhance the vegetation signal and to minimize the impact of aerosol perturbations by introducing a blue band:

$$EVI = G * (R_{NIR} - R_{RED})/(R_{NIR} + C1 * R_{RED} - C2 * R_{BLUE} + C3), \quad (4)$$

where G is the gain factor, and C1, C2, and C3 are the pixel-independent coefficients (for MODIS data, G = 2.5, C1 = 6, C2 = 7.5, C3 = 1). However, similar to NDVI, it also suffers, to a lesser extent, from influence of variable solar/viewing geometry, sun glint, and thin clouds when used to map floating macroalgae (Hu, 2009).

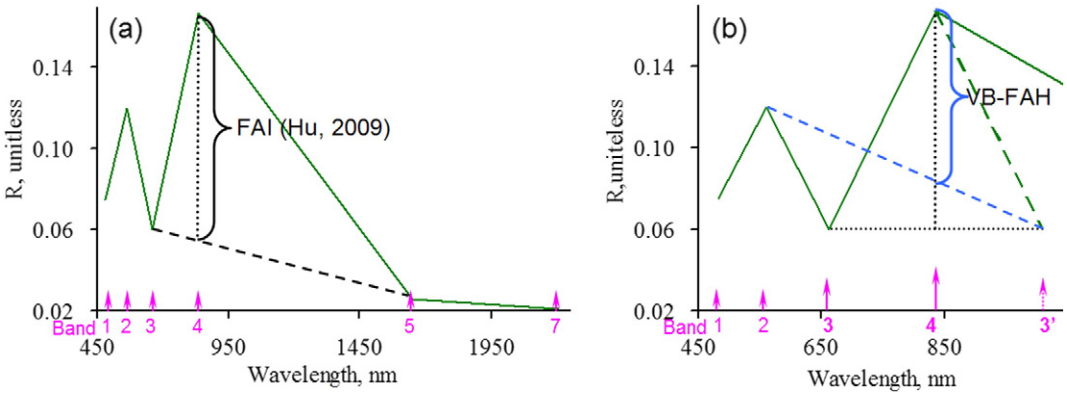

Fig. 2. Illustration of (a) the floating algae index — FAI (Hu, 2009) and (b) Virtual Baseline Floating macroAlgae Height (VB-FAH) using the same reflectance spectrum. In (b), the virtual Band 3′ is a mirror band of Band 3 symmetric to Band 4. These band numbers apply to both HJ-1 and Landsats 5 and 7.

To overcome these difficulties, Hu (2009) proposed a Floating Algae Index (FAI) using a baseline-subtraction approach:

$$FAI = (R_4 - R_3) + (R_3 - R_5) * (\lambda_4 - \lambda_3)/(\lambda_5 - \lambda_3), \quad (5)$$

where R is the reflectance, and λ is wavelength with subscript number representing the band number of Landsats 5 and 7.

The FAI uses two bands in the red and shortwave infrared (SWIR) to form a baseline, which is then subtracted from the near-infrared (NIR) reflectance. Such a subtraction takes care of perturbations from many sources, thus making it easier to establish image-independent thresholds to detect and quantify floating macroalgae although more sophisticated image segmentation methods have been proposed (e.g., Garcia, Fearns, Keesing, & Liu, 2013). For its simplicity and effectiveness, FAI has been applied to both MODIS and Landsat to study floating macroalgae as well as wetlands (e.g., Yu & Hu, 2013). However, this method cannot be applied to HJ-1 due to its lack of the SWIR band. Thus, an alternative approach must be developed to take the advantage of the FAI design in the absence of the SWIR band.

Here, based on the same principle of baseline subtraction approaches (e.g., FAI), a new index for mapping floating macroalgae is developed, which is named as Virtual-Baseline Floating macroAlgae Height (VB-FAH). The idea is to form a virtual baseline using the green and red bands, but the red band is artificially re-located to represent a SWIR band. Fig. 2 illustrates the concepts of both FAI and VB-FAH, where the arithmetic formula of VB-FAH is presented in Eq. (6):

$$VB\text{-}FAH = (R_4 - R_2) + (R_2 - R_3) * (\lambda_4 - \lambda_2)/(2\lambda_4 - \lambda_3 - \lambda_2). \quad (6)$$

As shown in Fig. 1c, floating macroalgae showed specific spectral features as follows: 1) higher NIR reflectance than over sea water; 2) higher NIR reflectance than in the red band (i.e., the red-edge vegetation reflectance), and 3) higher NIR sensitivity to floating macroalgae than the red and green bands. These characteristics form the basis of the VB-FAH design: while the NIR band is used to measure the height, the red and green bands serve as the baseline. This is similar to the FAI band-subtraction design (Hu, 2009), with the expectation that VB-FAH can partially remove the impacts of variable aerosols, solar/viewing geometry, and thin clouds. Because both Landsat and HJ-1 have the bands required by the VB-FAH, once this index is validated, a consistent time-series may be established using the two sensor series.

3.2. Validation of VB-FAH for MAB detection

The new VB-FAH index was evaluated in two ways. First, it was tested against the established FAI using data collected from the same Landsat sensor. Then, it was tested between HJ-1 and Landsat using the same VB-FAH. The purpose was to show that VB-FAH was equivalent to FAI, and was also consistent between sensors.

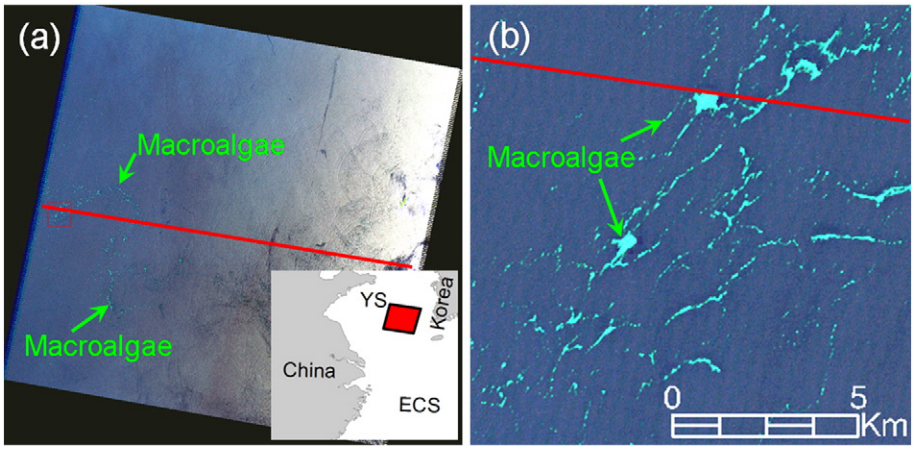

Fig. 3. (a) Landsat-5 Red-Green-Blue composite image by bands 7 (R, 2.08–2.35 μm), 4 (G, 0.76–0.90 μm) and 2 (B, 0.52–0.60 μm) acquired over the YS at 02:06:30 GMT on 24 June 2009, whose location is shown by the red quadrangle in the lower-right figure; (b) a zoomed area, whose location is shown in (a) as a red box, showing floating macroalgae in cyan color. The red line is an artificial cross-track transect.

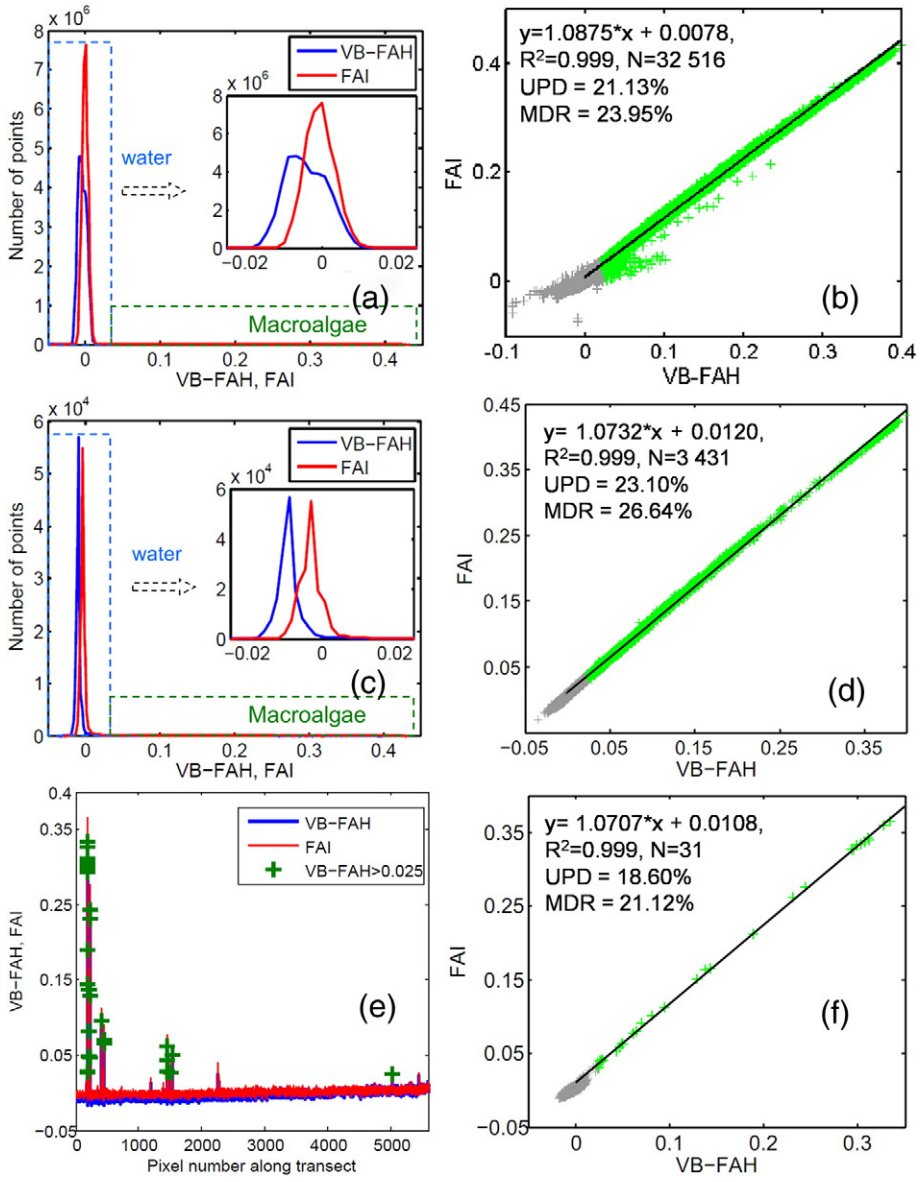

Fig. 4. Comparison between Landsat VB-FAH and FAI. (a) Frequency distributions of VB-FAH and FAI (FAI: min = −0.073, max = 0.433; VB-FAH: min = −0.091, max = 0.400. The step in the x-axis was calculated as (max − min) / 255; (b) their relationship over the entire image in Fig. 3a (the linear regression function, UPD, and MDR are for the green points with VB-FAH ≥ 0.025); (c) and (d) are for a small region shown in Fig. 3b (FAI: min = −0.030, max = 0.433; VB-FAH: min = −0.036, max = 0.400); (e) and (f), VB-FAH and FAI values for the pixels along the artificial transect in Fig. 3a.

3.2.1. Comparison between VB-FAH and FAI for MAB detection

Landsat-5 TM data acquired on 24 June 2009 during a MAB in the YS (Fig. 3) were processed to surface reflectance, FAI, and VB-FAH using the above-described methods. The Red-Green-Blue composite images can reveal floating macroalgae in a qualitative way, yet quantitative analysis requires the VB-FAH and FAI indices.

Fig. 4a shows the frequency distributions of VB-FAH and FAI over the entire image as shown in Fig. 3a. Both VB-FAH and FAI ranged from −0.1 to 0.5 with peaks near 0.0, and both had long tails in their frequency distributions. Furthermore, a linear relationship between VB-FAH and FAI was observed, especially for the pixels with VB-FAH ≥ 0.025 (i.e., pixels of macroalgae) (Fig. 4b, $R^2 = 0.999$, $N = 32.516$). For a smaller region covering the visually identified macroalgae slicks, Fig. 4c and d also shows similar distributions and linear relationship between VB-FAH and FAI (for pixels of macroalgae, $R^2 = 0.999$, $N = 3431$). For the artificial transect line across the entire image (Fig. 3a), Fig. 4e shows the VB-FAH and FAI values where the spikes were caused by macroalgae. Similar to the above results, a tight relationship was found between VB-FAH and FAI along this transect line (Fig. 4f, for pixels of macroalgae, $R^2 = 0.970$, $N = 31$). As shown in Fig. 4e, VB-FAH and FAI of macroalgae-free pixels along the cross-track transect had low variations, implying that both indices were not sensitive to variations in viewing geometry and changing aerosols (Hu, 2009). In contrast, the corresponding NDVI showed much higher variations along the same transect (not shown here), confirming the arguments of Hu (2009) that FAI was a better index. For the pixels containing floating macroalgae, UPD and MDR between FAI and VB-FAH were <22% and 24%, respectively, for the entire image.

While it is relatively easy to visualize the macroalgae slicks from either the RGB composite images or the VB-FAH images, determining a threshold to separate macroalgae-containing pixels from macroalgae-free pixels is not straightforward because 1) many pixels may be mixed with both water and macroalgae and 2) the macroalgae may be slightly submerged in water, causing decreased NIR reflectance. A higher

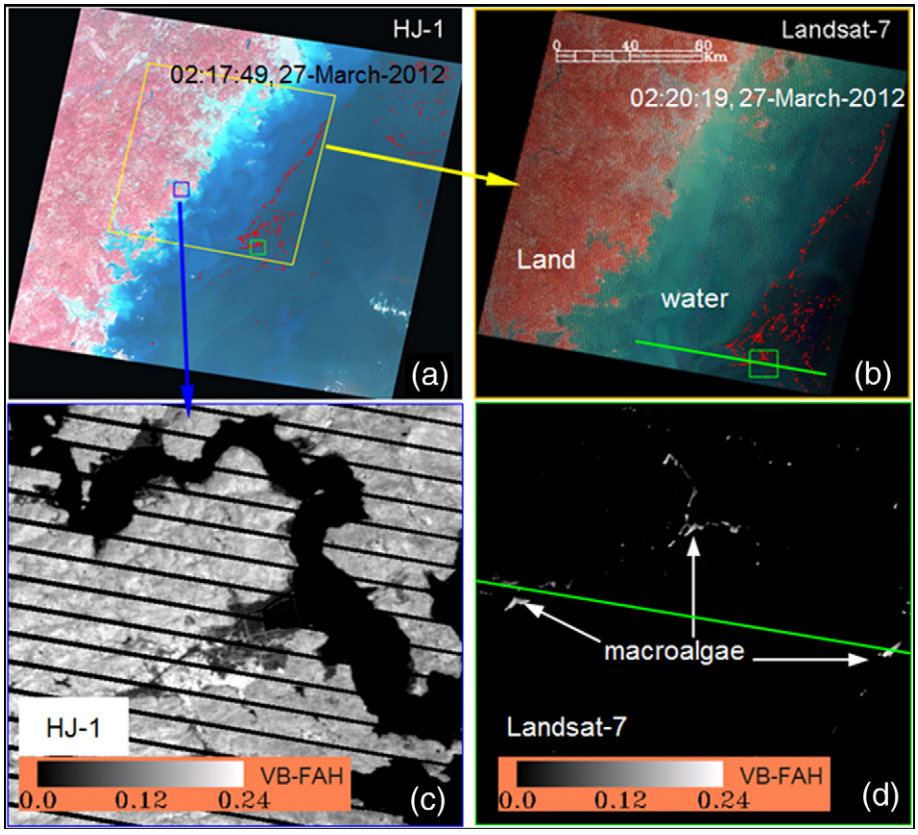

Fig. 5. (a) and (b) RGB composite images by HJ-1 and Landsat-7, respectively, on 27 March 2012. For the HJ-1 image, R is band 4 (0.76–0.90 μm), G is band 2 (0.52–0.60 μm), and B is band 1 (0.43–0.52 μm). The red slicks in (a) and (b) are pixels with VB-FAH (HJ-1) ≥ 0.025 and VB-FAH (Landsat-7) ≥ 0.038, respectively (see text for more details). (c) HJ-1 VB-FAH image of a coastal area (location shown as a blue box in (a)). To facilitate comparison with Landsat-7, the missing-data stripes from Landsat-7 are overlaid on this HJ-1 image. (d) Landsat-7 VB-FAH image of offshore waters with floating macroalgae shown as bright pixels. The image location is annotated as a green box in (a) and (b). The green line shows a cross-track transect.

threshold may lead to fewer pixels identified as macroalgae. Therefore, any choice of a fixed threshold will be a compromise. In this study, the threshold was selected based on the VB-FAH frequency distributions (Fig. 4, and those from other images shown in the next sections). From the VB-FAH frequency distributions, for macroalgae-free water pixels, the VB-FAH values were all <0.02 (inset in Fig. 4a). The long tails to the right were due to the presence of floating macroalgae. It is clear that the macroalgae-free water pixels have their VB-FAH values centered around 0.0 and lower than 0.02. To avoid possibility of identifying pure water pixels as macroalgae-containing pixels, the threshold was artificially lifted to 0.025. Although some sophisticated approaches might be used to optimize the threshold selection (e.g., Meng & Xing, 2013; Garcia, Fearns, Keesing, & Liu, 2013; Liu, Keesing, Xing, & Shi, 2009), the goal of this study was to provide a simple index to delineate macroalgae slicks. In practice, the delineated slicks were always visually inspected to assure the fidelity of the results (e.g., spectral shapes, slick morphology). It is also noted that the change of VB-FAH threshold from 0.02 to 0.025 had only small impact on the number

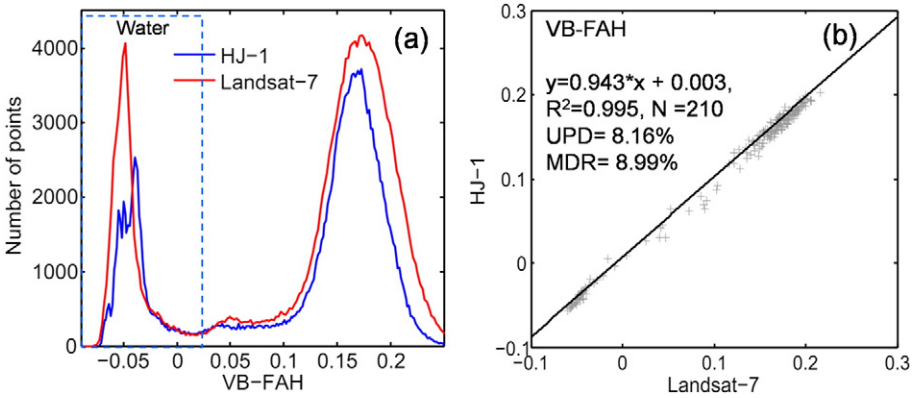

Fig. 6. (a) Frequency distributions of VB-FAH from concurrent HJ-1 (min = −0.0726, max = 0.309) and Landsat-7 (min = −0.157, max = 0.397) over a coastal zone including both land and water (area shown in Fig. 5c); (b) The same data from (a), but presented in x-y scatter plot. The pixels outside the dashed box in (a) are non-water pixels (including land vegetation). Please note that the size of pixel in the scatter plot (b) is 930 m * 930 m.

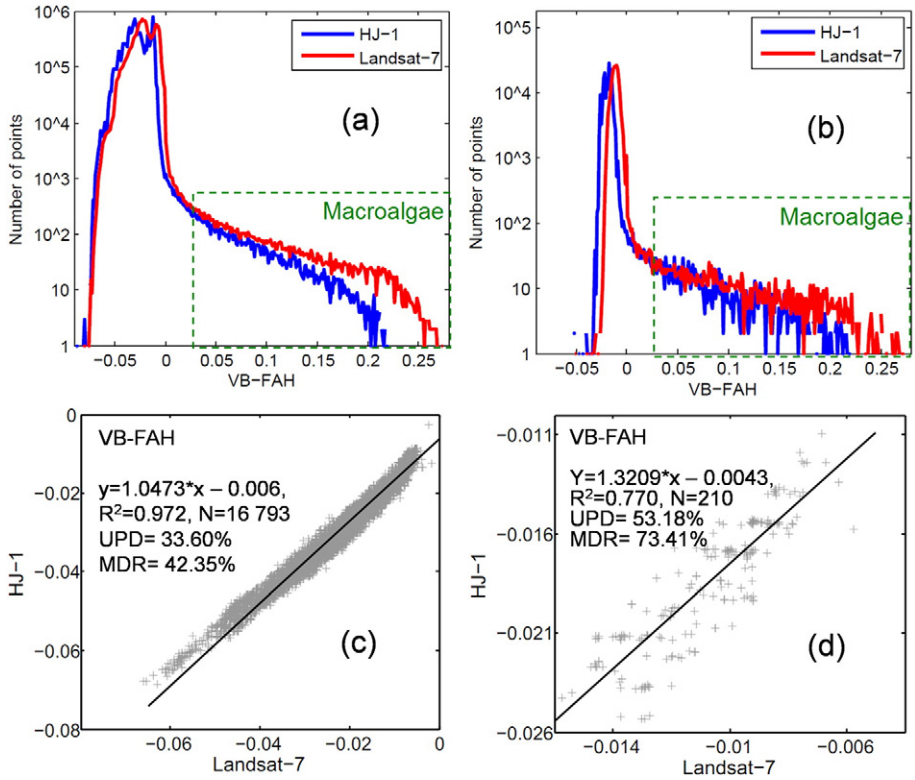

Fig. 7. (a) and (b) VB-FAH frequency distributions of HJ-1 and Landsat-7 for the regions shown in Fig. 5b and Fig. 5d, respectively. (c) and (d) the same data as shown in (a) and (b) but presented in x-y scatter plots. The statistics of the comparison are annotated in (c) and (d). Please also note that the size of pixel in the scatter plots (c) and (d) is 930 m * 930 m.

of classified macroalgae pixels (see Supplemental Fig. S1 for details). Thus, for this study a VB-FAH threshold of 0.025 was chosen to delineate macroalgae-containing pixels.

The above images were collected over relatively clear waters in the YS. Another set of Landsat-7 images acquired over turbid waters in the ECS (Figs. 1a and 5) were also analysed for their VB-FAH and FAI distributions, with similar results observed (i.e., tight linear relationship between FAI and VB-FAH, not shown here). These results suggest that in the absence of a SWIR band, VB-FAH can be used as an alternative to FAI to take its advantage of tolerance to environmental perturbations.

3.2.2. Comparison between HJ-1 and Landsat VB-FAH for MAB detection

A pair of concurrent HJ-1 and Landsat-7 image over coastal waters of the ECS (Fig. 1a) were used to study the consistency between their VB-FAH values. Fig. 5 shows the image pair acquired on the same day three minutes apart.

Fig. 6 shows the comparison between HJ-1 and Landsat-7 VB-FAH values for a small region containing both land and water (Fig. 5c). Cross-sensor consistency can be seen from either the frequency distributions in Fig. 6a or the x-y scatter plot in Fig. 6b for both the water pixels and the non-water pixels (including land vegetation). Note that to avoid errors induced by geo-referencing uncertainties and possible changes in water's reflectance caused by currents, waves and swells within 3 min, the 30-m pixels were aggregated to 930-m.

Similar to Fig. 6 for a small coastal zone, Fig. 7 shows the comparison between HJ-1 and Landsat-7 VB-FAH for the entire water region in Fig. 5b and for a selected small window in Fig. 5d. Excellent agreement between the two sensors is observed, where the small shift in the frequency distributions might be caused by radiometric calibration and atmospheric correction. However, such a shift would not impact the use of VB-FAH in quantifying floating macroalgae area coverage. For example, for the same region shown in Fig. 5d, if 0.025 is used as

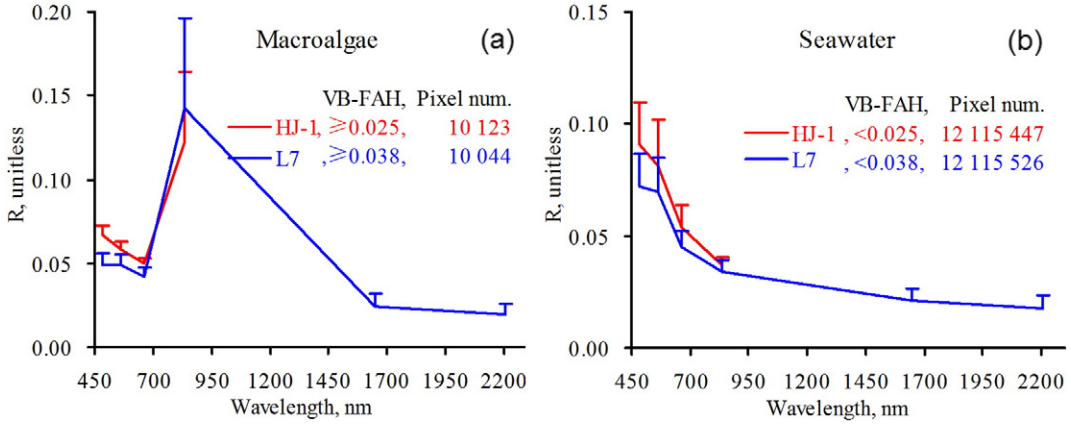

Fig. 8. Mean reflectance spectra of (a) floating macroalgae and (b) sea water extracted over the waters shown in Fig. 5b from Landsat-7 (L7) and HJ-1 images, respectively.

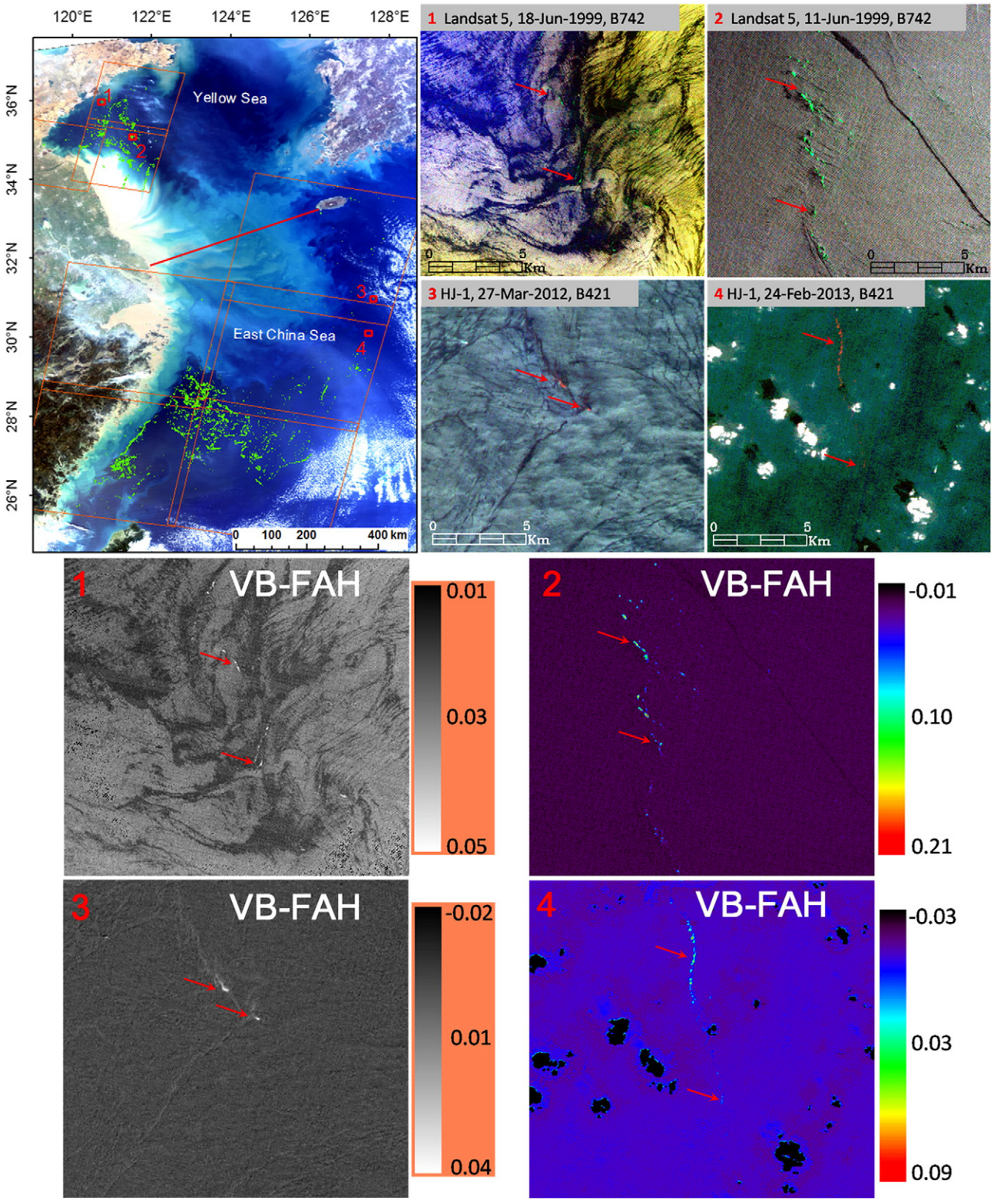

Fig. 9. Examples of floating macroalgae detected from Landsat images before 2007 and from HJ-1 images during the winter-spring season under various conditions. The numbered zoom-in images correspond to the red boxes shown on a background MODIS image to the left (27 March 2012). The red arrows indicate macroalgae pixels which appear as green color in the Landsat RGB composite image (R: band 7, G: band 4, B: band 2), red color in the HJ-1 RGB composite image (R: band 4, G: band 2, B: band 1); the corresponding VB-FAH images also showed the macroalgae pixels. The black patches in VB-FAH image numbered 4 are masks for clouds.

the threshold for HJ-1 and 0.038 for Landsat-7 (see Supplemental Fig. S1 for the threshold determination from the cumulative frequency plot), the classified macroalgae area coverage is very close between HJ-1 (10,123 pixels or 9.11 km^2) and Landsat-7 (10,044 pixels or 9.04 km^2), suggesting that a slight adjustment in the sensor-specific thresholds can be used to assure cross-sensor consistency. This is different from simple detection of macroalgae-containing pixels when studying historical bloom events, where a single threshold is usually

Table 2
MAB observations from Landsat VB-FAH images before 2007 in the southwestern part of the YS. Numbers in parentheses indicate areas of MAB (VB-FAH ≥ 0.025) for the Landsat scene P199R036 in the Worldwide Reference System-2 (see Fig. 9 for the location).

Year	Landsat dates, month/day (covering area of MAB, km^2)	MAB Observed? Yes (+) or no (−)
1995	05/22	−
1996	06/18, 07/08	−
1997	05/20, 06/21	−
1998	06/15, 07/10, 07/26	−
1999	06/11 (1.830)	+
2000	06/05 (0.760)	+
2001	05/31 (5.126)	+
2002	05/25, 07/12	−
2003	06/06, 06/13	−
2004	05/23 (0.210)	+
2005	06/02, 06/11	−
2006	05/29	−

sufficient. Note that the data scattering in Fig. 7d for a small region is likely caused by the cross-sensor mismatching between pixels due to potential geo-referencing errors. However, such data scattering did not appear to impact the image classification results shown in Fig. 5a and b for HJ-1 and Landsat-7, respectively. Indeed, mean reflectance spectra of classified macroalgae and seawater from HJ-1 and Lansat-7 showed excellent agreement (Fig. 8), also suggesting the compatibility of HJ-1 and Landsat in their VB-FAH for detecting and quantifying MABs. As shown in Fig. 8a, the HJ-1 reflectance after atmospheric correction through the FLAASH module showed typical spectral features of macroalgae, i.e., the high reflectance and variations in the NIR band and the strong absorption in the red band, which have been revealed by the in-situ measured macroalgae reflectance (see Fig. 1c).

4. MAB mapping results and discussions

Based on the above analysis, in the absence of a SWIR band, VB-FAH can be used as an alternative index to FAI to detect MABs, and such an index is consistent between HJ-1 and Landsat measurements. Thus, the index with a threshold of 0.025 was applied to both HJ-1 and Landsat data for detection of floating macroalgae and to study historical MAB events in the study region. Specifically, Landsat observations over the YS before 2007 were used to find the earliest possible MABs, and HJ-1 observations over the ECS after 2009 were searched for MABs during winter and spring of every year in order to detect early occurrence of MABs in this region. Without concurrent field data to validate the satellite-based observations, two criteria were used to verify the detected MABs. First, aggregation of floating macroalgae under winds and currents is featured by thin slicks or small patches (Hu, Feng, Hardy, & Hochberg, 2015; Hu, Li, Chen, Ge, Muller-Karger, Liu, Yu, & He, 2010; Hu, Yang, Zhang, Chen, & He, 2014; Dierssen, Chlus, & Russell, 2015). Floating macroalgae slicks were thus delineated on Landsat and HJ-1 VB-FAH images (VB-FAH ≥ 0.025), and then visualized on their corresponding color-composite images (Fig. 9). For the three composite bands used for the two sensors, MABs appear greenish in the Landsat composite images while reddish in the HJ-1 composite images (Fig. 9) where boxes 1# and 3# showed the typical feature of macroalgae aggregation in a plume front zone of coastal turbid waters and a flow convergence zone (Hu, Yang, Zhang, Chen, & He, 2014), respectively. Then, this morphological check was further verified by spectral analyses of randomly selected MAB pixels to compare their spectra against the spectral shapes shown in Fig. 8. The results are summarized below for Landsat and HJ-1, respectively.

Table 3
MAB observations from HJ-1 VB-FAH images covering the ECS in winter and spring since 2009. For each date, there are several HJ-1 scenes covering the ECS (locations shown in Fig. 10 as red rectangular boxes).

Year	HJ-1 dates, month/day (covering area of MAB, km^2)	Observed MAB? Yes (+) no (−)
2009	03/15, 03/31	−
2010	03/29	−
2011	03/28	−
2012	03/27 (54.95)	+
2013	02/24 (1.42), 03/06 (26.74), 03/08(17.26), 03/12 (8.50), 03/16 (7.34)	+
2014[a]	03/22 (0.19)	+

[a] Due to changes in the acquisition schedule, there were fewer HJ-1 images in spring 2014.

4.1. MAB occurrence in the YS before 2007 from Landsat observations

Table 2 lists Landsat-derived MABs in 1999, 2000, 2001, and 2004 in the YS; whenever MABs were present, their coverage was also estimated and listed in the parentheses. These detections are consistent with the observations of MAB occurrence in the YS before 2007 by Hu, Li, Chen, Ge, Muller-Karger, Liu, Yu, & He (2010), yet this analysis revealed MABs back to 1999 for the first time. Due to the scarcity of Landsat data and frequent cloud cover, no MAB was observed from Landsat images in 2002, 2003, 2005 or 2006, which however does not mean that there was no MAB in these years. In 1999, a MAB was observed from the Landsat scene P199R036 (Worldwide Reference System-2, Fig. 9), extending to cover the coastal waters near Qingdao (box #1 in Fig. 9). The Landsat-derived MABs in the YS were mainly located in the waters near the Jiangsu Shoal (JS, Fig. 1), suggesting the possible origin and south-north drifting path in summer (Xing, Hu, Tang, Tian, Tang, Wang, Lou, & Gao, 2015b). These Landsat-based results suggest that MABs in the YS can be traced as far back as 1999 although their magnitudes before 2006 were much smaller than those after 2007 (Hu, Li, Chen, Ge, Muller-Karger, Liu, Yu, & He, 2010; Xing, Tosi, Braga, Gao, & Gao, 2015a).

4.2. MAB occurrence in the ECS during winter and spring from HJ-1 observations after 2009

Table 3 shows that MABs were detected in the ECS from HJ-1 VB-FAH images in every March since 2012. MABs might also occur in previous years (2009–2011), but due to frequent cloud cover in this region, the limited HJ-1 images simply did not show them. The MAB impacted area on 27 March 2012 was visually estimated to be 200,000 km^2 with MABs covering about 55 km^2 of sea surface. Fig. 10 further shows that on this day the MAB extended south to 26°N, about 100 km away from Fujian Province and Taiwan, and extended east to the Kuroshio Current (KC) which was characterized by high Sea Surface Temperature (SST, 25 °C) (Fig. 10b). Such a large scale of MAB is comparable to those reported for the YS since 2007, and thus could be detected by 250-m or 500-m moderate-spatial-resolution sensors such as MODIS and GOCI (Son, Choi, Kim, & Park, 2015; Son, Min, & Ryu, 2012). With the presence of MABs, SST generally ranged between 13 and 23 °C, close to an optimal temperature range for macroalgae growth (Liu, Keesing, Xing, & Shi, 2009, and reference therein).

The results shown in Fig. 9 and Fig. 10a also indicate that the earliest small-scale MABs occurred in the month of February (24 February 2013) off the turbid plume of the Subei Coastal Current (SBCC) in the ECS, which expanded rapidly to the southwestern part of the ECS in the following 20 days. This observation is in good agreement with local circulations (see Supplemental Fig. S2), and also consistent with previous suggestions that floating macroalgae drifted from the JS to the ECS at the end of April and early May under the influence of the Subei Coastal Current (SBCC, Xing, Zheng, Shi, Hao, Yu, Liang, Liu, & Zhang, 2011).

4.3. Implications on the origins and causes of the MABs in the YS and the ECS

The above new data on the winter-spring MABs in the ECS and the long history of MABs in the YS, provide important temporal and spatial

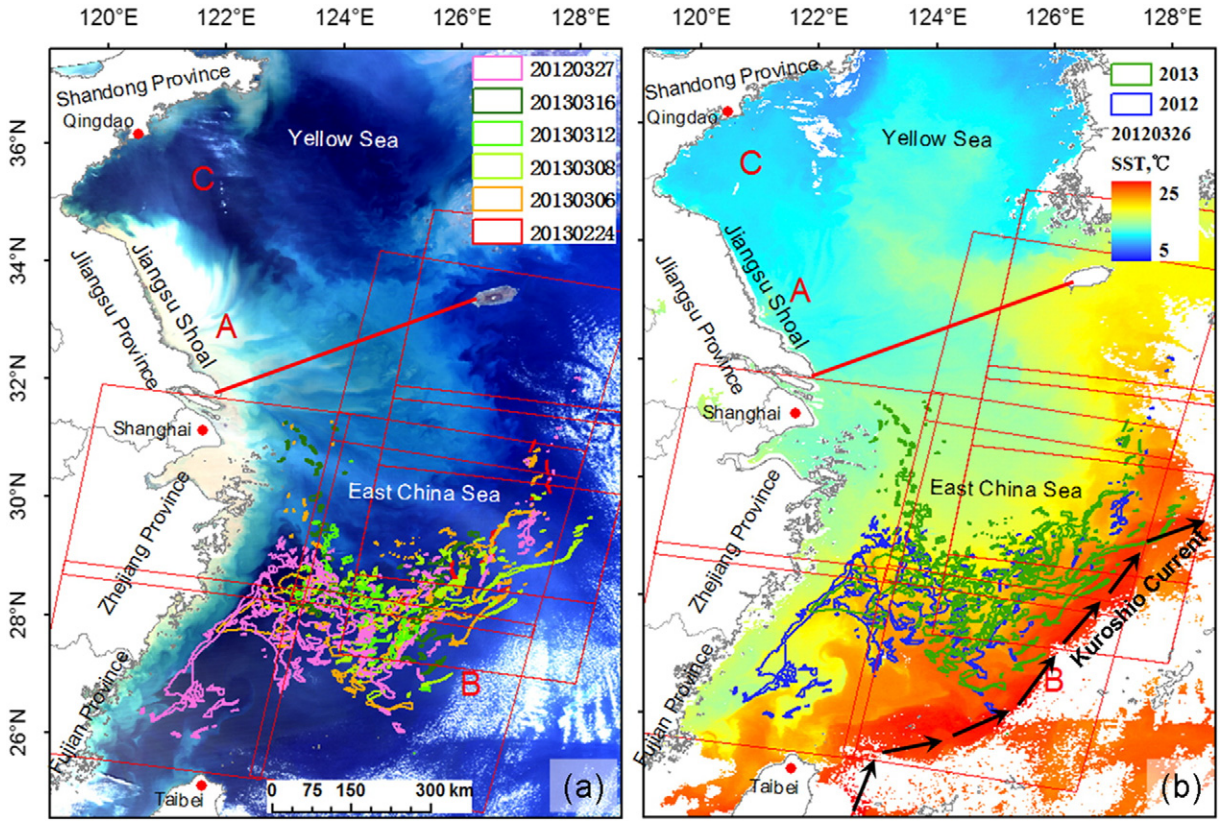

Fig. 10. MAB distributions in the ECS overlaid on a background MODIS RGB image (a) and SST image (b) acquired on 26 March 2012. The dates (in the format of YYYYMMDD) of the observed floating macroalgae slicks are color coded. Region A shows the Jiangsu Shoal, the source of the MABs in the YS as suggested by previous studies; Region B shows MAB locations in winter and spring revealed by this study; Region C shows the region of recurrent MABs in summer (see also Fig. 1). The black arrows in (b) show the pathway of the Kuroshio Current (KC).

information for exploring the origins, causes and consequences of MABs in this region. The JS is generally thought to be the origin of MAB seeds (Hu & He, 2008; Liu, Keesing, Xing, & Shi, 2009; Xing, Liu, Liang, Yu, & Shi, 2010; Xing, Loisel, Schmitt, Shi, Liu, & Keesing, 2009; Hu, Li, Chen, Ge, Muller-Karger, Liu, Yu, & He, 2010), but how the seeds are produced remains unclear. Liu, Keesing, Xing, & Shi (2009) suggested that they were from the "nori" (seaweed *Pyropia yezoensis*) farming facilities in the JS (Xing, Tosi, Braga, Gao, & Gao, 2015a): at the end of April (after the nori harvesting season) when the facilities (bamboo poles, ropes) were removed and recycled, the green macroalgae (*Ulva* spp.) growing on the facilities were also removed and deserted in the sea water, serving as the seed source of MABs (China Ocean News, CON, 2013; Wang, Xiao, Fan, Li, Liu, & Liu, 2015). An alternative explanation is that the seeds were released from the animal (crabs and prawns) aquaculture ponds in April (Pang, Liu, Shan, Xu, Zhang, Gao, Chopin, & Sun, 2010). However, these explanations are not adequate to explain why MABs occurred in March, February, and even January (e.g., in 2015, Xing, Wang, & Li, 2015c). The new observations of MABs in winter and spring since 2012 suggest that the origins and causes of MABs may need to be revisited.

There is a long history of harvesting green macroalgae for food in the Zhejiang Province (Wu, 1961). Green macroalgae grows naturally on eutrophicated tidal flats along the coast of Zhejiang Province, forming "grassland" during ebb tides. From December to next May, workers used rakes to scratch and collect the filamentous macroalgae during the low-tidal period (China Network Television, CNTV, 2011). However, this kind of human disturbance might not lead to the large amount of macroalgae seeds because the green macroalgae were collected rather than deserted. Considering the fact that the southward SBCC is not favorable for coastal waters of Zhejiang Province to move northward in winter, harvesting of green macroalgae in the Zhejiang Province is thus unlikely the reason of large-scale MABs in the YS and ECS. In contrast, human activities and/or environmental changes in the JS, become the key issues for exploring the origins and causes of MAB in the YS and the ECS.

The winter-spring MABs in 2012 in the ECS (Fig. 10), is in good agreement with the seasonal timing of a large-scale "rotten thallus" hazard in nori farm in the JS in November 2011 (China Fisheries Information, CFI, 2012), which led us to suspect that "rotten thallus" hazard induced the MABs. In the follow-on work, MABs were also observed to be present in the ECS in January 2015 with the "rotten thallus" hazard in the JS during the same winter (Xing, Wang, & Li, 2015c). "Rotten seedlings/thallus" hazards have frequently occurred with nori farming (Song, 2009; Lin, 2014). With these hazards, nori seedlings/thallus rotted; meanwhile, excessive green macroalgae (e.g., *Ulva* spp.) could replace nori (e.g., *Pyropia yezoensis*) and dominate farming facilities, and they were usually removed and deserted into sea water by farmers in the winter-spring period, which then might cause the winter-spring MABs as shown in Table 3. MABs in the year of 1999, 2004 (Table 2) as well as the well-known 2008, were also consistent with the timing of the reported historic "rotten seedlings/thallus" hazards (Song, 2009; Lv, Yan, Liu, Zhang, Wang, & Zheng, 2010), which supports the assumption that MABs might be induced by the "rotten seedling/thallus" hazards in nori farm.

5. Sensitivity of VB-FAH to variations in sea surface glint and aerosols

Sun glint and sky light caused by the Fresnel reflection on sea surface have strong impacts on the sea surface reflectance (Kutser, Vahtmäe, Paavel, & Kauer, 2013), especially for high resolution satellite images (Kay, Hedley, & Lavender, 2009; Lobo, Costa, & Novo, 2015) such as Landsat and HJ-1. Variations in sun glint might be one of major sources

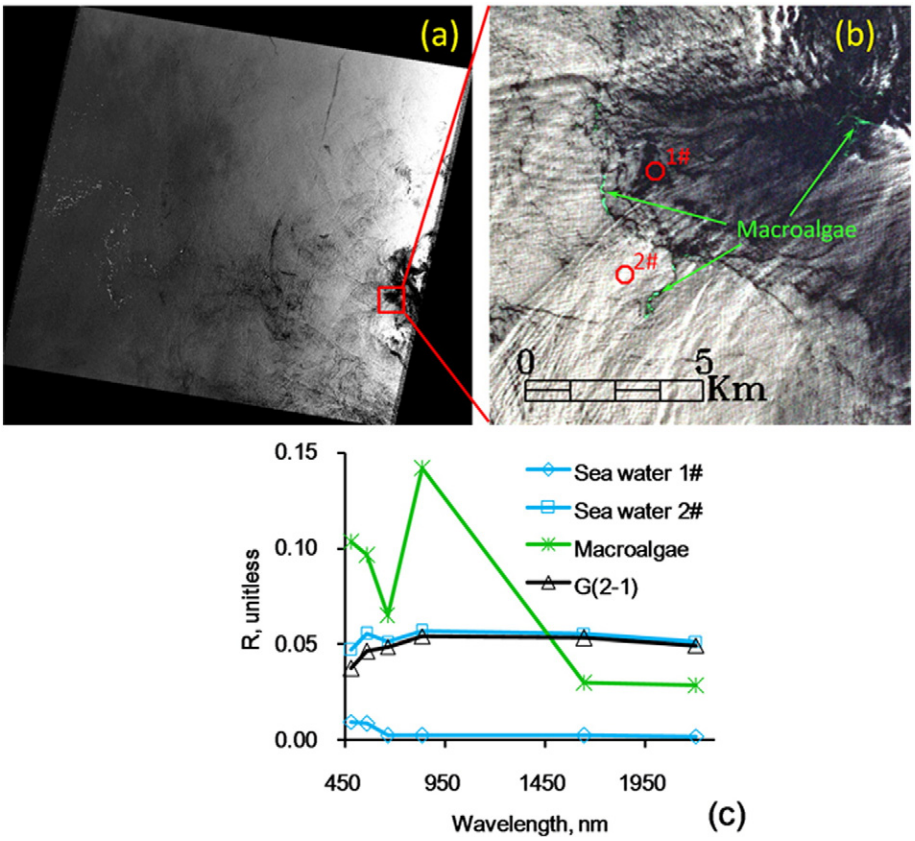

Fig. 11. (a) Band 4 reflectance image of Landsat-5 acquired on July 15, 2009 over the Yellow Sea. (b) A testing area with macroalgae and high dynamic range of glint; this image is a composite of bands 7, 4 and 2. (c) Reflectance of macroalgae (Rma) and sea water with low glint (Rsw1) and high glint (Rsw2), corresponding to the annotations in (b), respectively; G(2-1) refers to the reflectance difference (Rsw2 − Rsw1) between sites 1# and 2#.

causing uncertainties in using the FAI, VB-FAH, NDVI and NIR-RED (the vertical height extracted by the NIR and red bands, or the band difference, Richardson & Everitt, 1992) indexes to classify macroalgae pixels.

In order to investigate the effects of sun glint on macroalgae classification, a testing area in the YS (Fig. 11a) was selected. In the small area (Fig. 11b), there was a large dynamic range of glint intensity while variations in water constituents, viewing angles, and aerosols were negligible. Here the reflectance difference between Rsw1 and Rsw2 of sea water, i.e., G(2-1) = Rsw2 − Rsw1, was assumed to be due to sun glint. A sample spectrum of macroalgae (R) with maximum VB-FAH value was also selected to represent the macroalgae endmember. The indices of NDVI, NIR-RED, VB-FAH and FAI were calculated by using the variable portions of sun glint (G), and then normalized by their corresponding values from the macroalgae endmember spectrum.

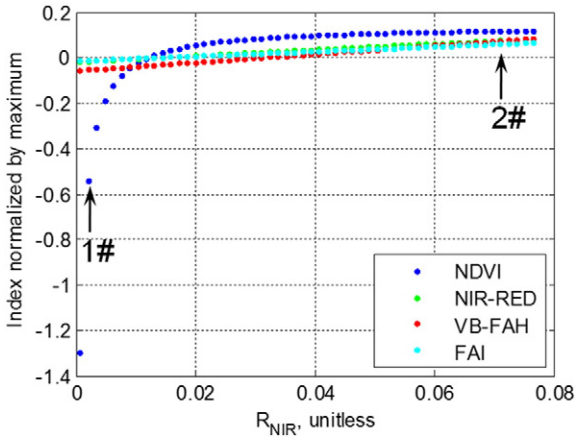

Fig. 12. Changes in NDVI, NIR-RED,VB-FAH, and FAI with the increase of glint, as indicated by the NIR reflectance. The indexes were all normalized by their maximums. The locations of sites 1# and 2# (see Fig. 11) are annotated with arrows.

As shown in Fig. 12, NDVI of sea water is sensitive to glint intensity when R_{NIR} is <0.02). In contrast, the three indices of NIR-RED, VB-FAH and FAI are much less sensitive to the same glint changes. Similar result was also obtained when the indexes were calculated from the top-of-atmosphere reflectance (R_{TOA}) (see Supplemental Fig. S3). Test of these indexes from Landsat images (Figs. 3 and 5) and HJ-1 images (see Supplemental Figs. S4, S5, and S6) also showed the same results. Although the simulation is for macroalgae-free pixels, because macroalgae can be slightly submerged in water or mixed with water in a 30-m pixel, the findings may also be applicable to macroalgae pixels.

Fig. 13a further shows that over sea surface with less variations in glint, VB-FAH of macroalgae pixels had a stable, monotonical nonlinear or linear relationship with NDVI, NIR-RED and FAI. However, over rough sea surface with high variations in glint (Fig. 13b), the non-linear relationship between VB-FAH and NDVI fell apart.

Hu (2009) showed the advantage of FAI over NDVI in mitigating the impacts caused by aerosol variations. Here, although atmospheric correction was performed using the FLAASH module, constant aerosol type and thickness were applied to the entire image, thus leaving the aerosol variations uncorrected. Although a radiative-transfer based simulation similar to that used in Hu (2009) was not carried out in this study, preliminary examples using image comparison showed that the VB-FAH appeared to be less sensitive than NDVI to aerosol variations (Supplemental Figs. S7 and S8). However, more work is still required to further demonstrate the sensitivity of VB-FAH to aerosol perturbations as well as to changes in the observing geometry.

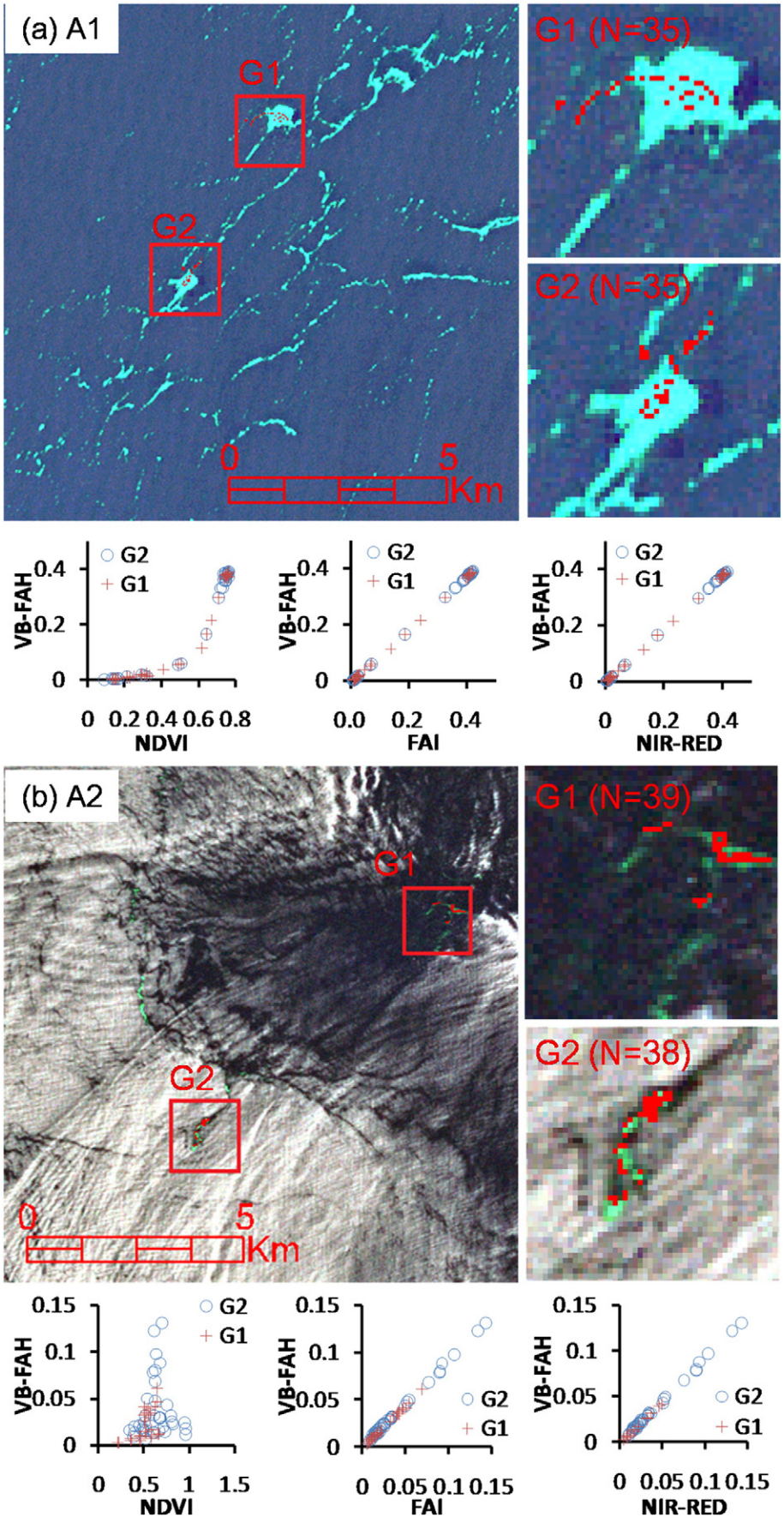
(a) A1
G1
G2
0
5
Km
G1 (N=35)
G2 (N=35)
VB-FAH
NDVI
FAI
NIR-RED
G2
G1
(b) A2
G1 (N=39)
G2 (N=38)

6. Application of VB-FAH to other sensors

It is not new to use a baseline subtraction to derive certain geophysical parameters from remote sensing. Ma, Xing, Chen, Zhang, Yu, & Shi (2011) used a peak-above-baseline method to retrieve suspended sediment concentrations in estuarine waters. Gitelson (1992) and Gitelson & Yacobi (2004) proposed a peak height and peak area model for Chl-a retrievals. Fluorescence Line Height (FLH, Letelier & Abott, 1996; Gower, Doerffer, & Borstad, 1999) and Maximum Chlorophyll Index (MCI, Gower, King, Borstad, & Brown, 2005) are also typical baseline techniques for Chl-a retrievals. MCI was also used to identifying floating macroalgae of *Sargassum* spp. (brown macroalgae) in the Gulf of Mexico and the Atlantic (Gower, Hu, Borstad, & King, 2006; Gower, Young, & King, 2013). Line depth is another type of baseline technique, for example the line depth around 620 nm was proposed by Dekker (1993) and Qi, Hu, Duan, Cannizzaro, & Ma (2014) for retrievals of phycocyanin pigments (rich in cyanobacteria), and the line depth around 675 nm was proposed by Xing, Lou, Chen, & Shi (2013a) to quantify Chl-a in sediments of emerged tidal flat.

All these traditional baseline techniques use different band positions for different sensors and purposes, with one thing in common: two bands surrounding the reference band are used to form the baseline, and the baseline subtraction is similar to the derivative techniques (Philpot, 1991; Han & Rundquist, 1997; Xing, Yu, Lou, Lü, Li, & Han, 2013b). Such a requirement of two neighboring bands cannot always be met for certain satellite sensors, for example, HJ-1A/B, QuickBird, and Rapid Eye where there is a lack of a SWIR band to form the baseline.

Such a difficulty may be overcome by the new concept of VB-FAH, as demonstrated above. Comparison of VB-FAH with NDVI showed significantly improved performance in terms of tolerance to perturbations from sea surface glint and aerosols. This study suggests that VB-FAH is a better index than NDVI in the absence of a SWIR band, thus may be extended to other sensors. We expect to test this concept over other sensors in the near future.

Finally, we want to emphasize that the proposed VB-FAH is one way to improve over NDVI to detect and quantify macroalgae in the absence of a SWIR band, but perhaps not the only way. Indeed, the NIR-RED band difference index, as proposed by Richardson & Everitt (1992), also showed similar performance as VB-FAH (Figs. 12, 13), suggesting that NIR-RED may be another reliable index for the purpose of detecting and quantifying macroalgae.

7. Concluding remarks

Due to the lack of a SWIR band, the design of FAI for mapping macroalgal blooms could not be extended to the HJ-1 sensors even though these sensors have the advantage over Landsat sensors in terms of spatial coverage and re-visit frequency. By converting a red band to a virtual SWIR band, a new index, namely the Virtual-Baseline Floating macroAlgae Height (VB-FAH), was developed in this study to examine the line height in the NIR. Comparison with other popular indexes showed that for the limited cases here VB-FAH appeared to be comparable to FAI but more advantageous over NDVI in terms of tolerance to perturbations from sun glint and possibly from aerosols, thus could possibly be extended to other high-resolution sensors (e.g., QuickBird, Rapid Eye) that are not equipped with a SWIR band.

The new VB-FAH was applied to HJ-1 measurements over the ECS, which revealed early occurrence of MABs in winter and early spring since 2012. Application of the VB-FAH to Landsat measurements over the southwestern part of the YS also showed MABs as early as 1999. These new findings provide important background knowledge for exploring the origins, causes, and consequences of MABs in the YS and the ECS.

Acknowledgements

This work was supported by the Chinese Academy of Sciences (XDA11020403, KZCX2-YW-Q07-01) and Shandong Province Scientific Innovative Program (2007GG2QT06019). Landsat images in this study are from USGS; HJ-1A/B images are from CRESDA. We especially thank Mingjing LOU, Dingfeng YU and Lingling WU for measuring the green macroalgae spectra, and thank Dr. Jiajia HAO from the Qingdao Institute of Oceanology (Chinese Academy of Sciences) for providing the data of local currents. Comments and suggestions from three anonymous reviewers helped to improve this manuscript.

Appendix A. Supplementary data

Supplementary data to this article can be found online at http://dx.doi.org/10.1016/j.rse.2016.02.065.

References

Barnes, B. B., & Hu, C. (2015). Cross-sensor continuity of satellite-derived water clarity in the Gulf of Mexico: Insights into temporal aliasing and implications for long-term water clarity assessment. *IEEE Transactions on Geoscience and Remote Sensing, 53*, 1761–1772.

China Fisheries Information (CFI) (2012). http://www.fishfirst.cn/article-9040-1.html

China Network Television (CNTV) (2011). http://sannong.cntv.cn/program/zhifujing/20110323/111001.shtml

China Ocean News (CON) (2013). http://www.oceanol.com/keji/kjdt/30433.html (2013-12-26)

Cui, T. -W., Zhang, J., Sun, L. -E., Jia, Y. -J., Zhao, W., Wang, Z. -L., & Meng, J. -M. (2013). Satellite monitoring of massive green macroalgae bloom (GMB): Imaging ability comparison of multi-source data and drifting velocity estimation. *Internal Journal of Remote Sensing, 33*, 5513–5527.

Dekker, A. G. (1993). *Detection of optical water quality parameters for eutrophic waters by high resolution remote sensing*. Netherlands: Vrije Universitei.

Dierssen, H. M., Chlus, A., & Russell, B. (2015). Hyperspectral discrimination of floating mats of seagrass wrack and the macroalgae *Sargassum* in coastal waters of Greater Florida Bay using airborne remote sensing. *Remote Sensing of Environment, 167*, 247–258.

Garcia, R., Fearns, P., Keesing, J. K., & Liu, D. (2013). Quantification of floating macroalgae blooms using the scaled algae index. *Journal of Geophysical Research: Oceans, 118*, 26–42.

Gower, J., King, S., Borstad, G., & Brown, L. (2005). Detection of intense plankton blooms using the 709 nm band of the MERIS imaging spectrometer. *International Journal of Remote Sensing, 26*, 2005–2012.

Gower, J., Doerffer, R., & Borstad, G. (1999). Interpretation of the 685 nm peak in water-leaving radiance spectra in terms of fluorescence, absorption and scattering, and its observation by MERIS. *Journal of Remote Sensing, 20*, 1771.

Gower, J., Hu, C., Borstad, G., & King, S. (2006). Ocean color satellites show extensive lines of floating Sargassum in the Gulf of Mexico. *IEEE Transactions on Geoscience and Remote Sensing, 44*, 3619–3625.

Gower, J., Young, E., & King, S. (2013). Satellite images suggest a new Sargassum source region in 2011. *Remote Sensing Letters, 4*, 764–773.

Gitelson, A. (1992). The peak near 700 nm on radiance spectra of algae and water — Relationships of its magnitude and position with chlorophyll concentration. *International Journal of Remote Sensing, 13*(17), 3367–3373.

Gitelson, A., & Yacobi, Y. (2004). Monitoring quality Of productive aquatic ecosystem: Requirements for satellite sensors. *BALWOIS 2004 Ohrid, FY Republic of Macedonia, 25–29 May 2004*.

Han, L., & Rundquist, D. C. (1997). Comparison of NIR/RED ratio and first derivative of reflectance in estimating algal-chlorophyll concentration: A case study in a turbid reservoir. *Remote Sensing of Environment, 62*(3), 253–261.

Hu, C., & He, M. X. (2008). Origin and offshore extent of floating algae in Olympic sailing area. *Eos Transactions AGU, 89*, 302–303.

Hu, C. (2009). A novel ocean color index to detect floating algae in the global oceans. *Remote Sensing of Environment, 113*, 2118–2129.

Hu, C., Li, D., Chen, C., Ge, J., Muller-Karger, F. E., Liu, J., ... He, M. -X. (2010). On the recurrent *Ulva prolifera* blooms in the Yellow Sea and East China Sea. *Journal of Geophysical Research, 115*, C05017. http://dx.doi.org/10.1029/2009JC005561.

Hu, C., Feng, L., Hardy, R. F., & Hochberg, E. J. (2015). Spectral and spatial requirements of remote measurements of pelagic Sargassum macroalgae. *Remote Sensing of Environment, 167*, 229–246.

Fig. 13. Scattering plots showing relationships between VB-FAH and NDVI, NIR-RED, FAI of macroalgae pixels in two areas: (a) A1 and (b) A2 with low and high variations in glint levels, respectively. Two groups of red pixels (macroalgae pixels) in each area were manually-selected (G1 and G2). A1 and A2 are the same as those shown in Fig.3b and Fig.11b, respectively.

Hu, S., Yang, H., Zhang, J., Chen, C., & He, P. (2014). Small-scale early aggregation of green tide macroalgae observed on the Subei Bank, Yellow Sea. *Marine Pollution Bulletin*, *81*, 166–173.

Huete, A. R., & Justice, C. (1999). *MODIS vegetation index (MOD13) algorithm theoretical basis document Ver. 3. 1999.*

Kay, S., Hedley, J. D., & Lavender, S. (2009). Sun glint correction of high and low spatial resolution images of aquatic scenes: A review of methods for visible and near-infrared wavelengths. *Remote Sensing*, *1*, 697–730.

Kaufman, Y. J., Wald, A., Remer, L. A., Gao, B., Li, R., & Flynn, L. (1997). The MODIS 2.1 lm channel-correlation with visible reflectance for use in remote sensing of aerosol. *IEEE Transactions on Geoscience and Remote Sensing*, *35*, 1–13.

Kutser, T. (2012). The possibility of using the Landsat image archive for monitoring long time trends in coloured dissolved organic matter concentration in lake waters. *Remote Sensing of Environment*, *123*, 334–338.

Kutser, T., Pierson, D. C., Kallio, K. Y., Reinart, A., & Sobek, S. (2004). Mapping lake CDOM by satellite remote sensing. *Remote Sensing of Environment*, *94*(4), 535–540.

Kutser, T., Vahtmäe, E., Paavel, B., & Kauer, T. (2013). Removing glint effects from field radiometry data measured in optically complex coastal and inland waters. *Remote Sensing of Environment*, *133*, 85–89.

Letelier, R. M., & Abott, M. R. (1996). An analysis of chlorophyll fluorescence algorithms for the Moderate Resolution Imaging Spectrometer (MODIS). *Remote Sensing of Environment*, *58*, 215–223.

Lin, X. -M. (2014). Primary study on the reasons for the rotten thallus of Porphyra haitanensis from Fuding Minzao Bay. *Journal of Fujian Fisheries*, *36*, 227–233.

Liu, D., Keesing, J. K., Xing, Q., & Shi, P. (2009). World's largest macroalgal bloom caused by expansion of seaweed aquaculture in China. *Marine Pollution Bulletin*. http://dx.doi.org/10.1016/j.marpolbul.2009.01.013.

Lobo, F. L., Costa, M. P. F., & Novo, E. M. L. M. (2015). Time-series analysis of Landsat-MSS/TM/OLI images over Amazonian waters impacted by gold mining activities. *Remote Sensing of Environment*, *157*, 170–184.

Lv, F., Yan, X. -H., Liu, C. -J., Zhang, P., Wang, T. -G., & Zheng, Y. -B. (2010). Selection of a high-temperature tolerant strain of *Porphyra haitanensis* and its cultivation in sea area. *Journal of Shanghai Ocean University*, *19*, 457–462.

Lyons, D. A., Arvanitidis, C., Blight, A. J., Chatzinikolaou, E., Guy-Haim, T., Kotta, J., ... Crowe, T. P. (2014). Macroalgal blooms alter community structure and primary productivity in marine ecosystems. *Global Change Biology*. http://dx.doi.org/10.1111/gcb.12644.

Ma, W., Xing, Q., Chen, C., Zhang, Y., Yu, D., & Shi, P. (2011). Using normalized peak area of remote sensing reflectance in the near-infrared region to estimate total suspended matter. *International Journal of Remote Sensing*, *32*(22), 7479–7486.

Meng, R., & Xing, Q. (2013). Detection of offshore ship and well platform based on optical remote sensing images. *Journal of Computer Applications*, *33*, 708–711.

Moses, W. J., Gitelson, A. A., Perk, R. L., Gurlin, D., Rundquist, D. C., Leavitt, B. C., ... Brakhage, P. (2012). Estimation of chlorophyll-a concentration in turbid productive waters using airborne hyperspectral data. *Water Research*, *46*(4), 993–1004.

Naimie, C. E., Blain, C. A., & Lynch, D. R. (2001). Seasonal mean circulation in the Yellow Sea — a model generated climatology. *Continental Shelf Research*, *21*, 667–695.

Pang, S. J., Liu, F., Shan, T. F., Xu, N., Zhang, Z. H., Gao, S. Q., ... Sun, S. (2010). Tracking the algal origin of the Ulva bloom in the Yellow Sea by a combination of molecular, morphological and physiological analyses. *Marine Environmental Research*, *69*, 207–215.

Philpot, W. D. (1991). The derivative ratio algorithm: Avoiding atmospheric effects in remote sensing. *IEEE Transactions on Geoscience and Remote Sensing*, *29*(3), 350–357.

Qi, L., Hu, C., Duan, H., Cannizzaro, J., & Ma, R. (2014). A novel MERIS algorithm to derive cyanobacterial phycocyanin pigment concentrations in a eutrophic lake: Theoretical basis and practical considerations. *Remote Sensing of Environment*, *154*, 298–317.

Richardson, A. J., & Everitt, J. H. (1992). Using spectral vegetation indices to estimate rangeland productivity. *Geocarto International*, *7*(1), 63–69.

Rouse, J. W., Haas, R. H., Schell, J. A., & Deering, D. W. (1973). Monitoring vegetation systems in the Great Plains with ERTS. *Third ERTS Symposium, NASA SP-351 I* (pp. 309–317).

Smetacek, V., & Zingone, A. (2013). Green and golden seaweed tides on the rise. *Nature*, *504*, 84–88.

Son, Y. B., Min, J. -E., & Ryu, J. -H. (2012). Detecting massive green algae (*Ulva prolifera*) blooms in the Yellow Sea and East China Sea using Geostationary Ocean Color Imager (GOCI) data. *Ocean Science Journal*, *47*(3), 359–375.

Son, Y. B., Choi, B. -J., Kim, Y. H., & Park, Y. -G. (2015). Tracing floating green algae blooms in the Yellow Sea and the East China Sea using GOCI satellite data and Lagrangian transport simulations. *Remote Sensing of Environment*, *156*, 21–33.

Song, W. -L. (2009). Analysis on rotten seedlings of *Porphyra haitanensis* and its prevention method. *Journal of Fujian Fisheries*, *6*, 72–75.

Su, J. (1998). Circulation dynamics of the China Seas North of 18 N. In A. R. Robinson, & K. H. Brink (Eds.), *The sea. Vol. 11*. (pp. 483–505). New York: Wiley.

Tian, L., Lu, J., Chen, X., Yu, Z., Xiao, J., Qiu, F., & Zhao, X. (2010). Atmospheric correction of HJ-1 A/B CCD images over Chinese coastal waters using MODIS-Terra aerosol data. *SCIENCE CHINA Technological Sciences*, *53*(1), 191–195.

Wang, Z., Xiao, J., Fan, S., Li, Y., Liu, X., & Liu, D. (2015). Who made the world's largest green tide in China?—An integrated study on the initiation and early development of the green tide in Yellow Sea. *Limnology and Oceanography*. http://dx.doi.org/10.1002/lno.10083.

Wu, S. (1961). The preliminary investigation of Enteromorpha at the Xiangshan harbor. *Journal of Zhejiang Agricultural Sciences*, *12*, 587–588.

Xing, Q., Loisel, H., Schmitt, F., Shi, P., Liu, D., & Keesing, J. (2009). *Detection of the green tide at the Yellow Sea and tracking its wind-forced drifting by remote sensing, Geophysical Research Abstracts 11, EGU2009-577, EGU General Assembly 2009, Vienna.*

Xing, Q., Liu, D., Liang, S., Yu, D., & Shi, P. (2010). Remote sensing of the transportation of green tide from the aquaculture area of the northern Jiangsu coast to Qingdao of Shandong. *Environmental Impact Assessment in China*, *12*, 10–14.

Xing, Q., Yu, D., Lou, M., Lü, Y., Li, S., & Han, Q. (2013b). Using in-situ reflectance to monitor the chlorophyll concentration in the surface layer of tidal flat. *Spectroscopy and Spectral Analysis*, *33*(8), 2188–2191.

Xing, Q., Lou, M., Chen, C., & Shi, P. (2013a). Using in situ and satellite hyperspectral data to estimate the surface suspended sediments concentrations in the Pearl River Estuary. *IEEE Journal of Selected Topics in Applied Earth Observations and Remote Sensing*. http://dx.doi.org/10.1109/JSTARS.2013.2238659.

Xing, Q., Zheng, X., Shi, P., Hao, J., Yu, D., Liang, S., ... Zhang, Y. (2011). Monitoring "Green Tide" in the Yellow Sea and the East China Sea using multi-temporal and multi-source remote sensing images. *Spectroscopy and Spectral Analysis*, *31*, 1644–1647.

Xing, Q., Tosi, L., Braga, F., Gao, X., & Gao, M. (2015a). Interpreting the progressive eutrophication behind the world's largest macroalgal blooms with water quality and ocean color data. *Natural Hazards*, *78*, 7–21.

Xing, Q., Hu, C., Tang, D., Tian, L., Tang, S., Wang, X. H., ... Gao, X. (2015b). World's largest macroalgal blooms altered phytoplankton biomass in summer in the Yellow Sea: Satellite observations. *Remote Sensing*, *7*, 12297–12313.

Xing, Q., Wang, X., & Li, L. (2015c). Detection of winter macroalgal blooms (2014–2015) in the East China Sea using HJ-1 and Landsat data. *Workshop program and book of abstracts of the 7th International Workshop on Modeling the Ocean, 1–5 June 2015, Canberra, Australia* (pp. 42).

Yu, K., & Hu, C. (2013). Changes in vegetative coverage of the Hongze Lake national wetland nature reserve: A decade-long assessment using MODIS medium-resolution data. *Journal of Applied Remote Sensing*, *7*(1), 073589. http://dx.doi.org/10.1117/1.JRS.7.073589.

Zeng, Q., Zhao, Y., Tian, L. -Q., & Chen, X. -L. (2013). Evaluation on the atmospheric correction methods for water color remote sensing by using HJ-1A/1B CCD image-taking Poyang Lake in China as a case. *Spectroscopy and Spectral Analysis*, *33*, 1320–1326.